

DOI:

<https://doi.org/10.1016/j.jqsrt.2017.01.016>

Attribution-NonCommercial-NoDerivatives 4.0 International (CC BY-NC-ND 4.0)

<https://creativecommons.org/licenses/by-nc-nd/4.0/>

Access to this work was provided by the University of Maryland, Baltimore County (UMBC) ScholarWorks@UMBC digital repository on the Maryland Shared Open Access (MD-SOAR) platform.

**Please provide feedback**

Please support the ScholarWorks@UMBC repository by emailing [scholarworks-group@umbc.edu](mailto:scholarworks-group@umbc.edu) and telling us what having access to this work means to you and why it's important to you. Thank you.



# Effects of ice crystal surface roughness and air bubble inclusions on cirrus cloud radiative properties from remote sensing perspective



Guanglin Tang<sup>a,\*</sup>, R. Lee Panetta<sup>a,c</sup>, Ping Yang<sup>a,b</sup>, George W. Kattawar<sup>b,d</sup>, Peng-Wang Zhai<sup>e</sup>

<sup>a</sup> Department of Atmospheric Sciences, Texas A&M University, College Station, TX, USA

<sup>b</sup> Department of Physics & Astronomy, Texas A&M University, College Station, TX, USA

<sup>c</sup> Department of Mathematics, Texas A&M University, College Station, TX, USA

<sup>d</sup> Institute for Quantum Science and Engineering, Texas A&M University, College Station, TX, USA

<sup>e</sup> Department of Physics, University of Maryland, Baltimore County, MD, USA

## ARTICLE INFO

### Article history:

Received 21 July 2016

Received in revised form

11 January 2017

Accepted 11 January 2017

Available online 17 January 2017

### Keywords:

Ice crystals

Surface roughness

Inhomogeneity

Air bubbles

Scattering

## ABSTRACT

We study the combined effects of surface roughness and inhomogeneity on the optical scattering properties of ice crystals and explore the consequent implications to remote sensing of cirrus cloud properties. Specifically, surface roughness and inhomogeneity are added to the Moderate Resolution Imaging Spectroradiometer (MODIS) collection 6 (MC6) cirrus cloud particle habit model. Light scattering properties of the new habit model are simulated using a modified version of the Improved Geometric Optics Method (IGOM). Both inhomogeneity and surface roughness affect the single scattering properties significantly. In visible bands, inhomogeneity and surface roughness both tend to smooth the phase function and eliminate halos and the backscattering peak. The asymmetry parameter varies with the degree of surface roughness following a U shape - decreases and then increases - with a minimum at around 0.15, whereas it decreases monotonically with the air bubble volume fraction. Air bubble inclusions significantly increase phase matrix element  $-P_{12}$  for scattering angles between  $20^\circ$ – $120^\circ$ , whereas surface roughness has a much weaker effect, increasing  $-P_{12}$  slightly from  $60^\circ$ – $120^\circ$ . Radiative transfer simulations and cirrus cloud property retrievals are conducted by including both the factors. In terms of surface roughness and air bubble volume fraction, retrievals of cirrus cloud optical thickness or the asymmetry parameter using solar bands show similar patterns of variation. Polarimetric simulations using the MC6 cirrus cloud particle habit model are shown to be more consistent with observations when both surface roughness and inhomogeneity are simultaneously considered.

© 2017 Elsevier Ltd. All rights reserved.

## 1. Introduction

The large uncertainties about the effects of cirrus cloud radiative forcing and feedbacks on global climate change motivate extensive studies of cirrus cloud properties [1]. In particular, reducing the uncertainties requires a better understanding of the optical properties of cirrus cloud particles, which are fundamental to remote sensing of bulk cirrus cloud properties and to the simulations of cirrus cloud radiative forcing and feedbacks [2,3]. The optical properties of pure ice crystals depend on particle shape and size. Generally speaking, the maximum dimension of ice crystals in cirrus clouds are in the range 5–600  $\mu\text{m}$  [4,5]. Particles can be either pristine ice crystals as small as several microns or aggregates as large as several hundred microns. The average size of bulk cirrus cloud particles is usually in the range of tens to

hundreds of microns [6]. In the case of visible solar radiation in the spectral region 0.3–0.7  $\mu\text{m}$ , the wavelengths are much smaller than the average cirrus cloud particle size. As a result, the optical properties of cirrus cloud particles are sensitive to particle shape [7–10] and surface roughness [11–15].

The MODIS product provides retrievals of cirrus cloud properties such as optical thickness, cloud top pressure and effective radius using multiple MODIS bands [16]. A previous MODIS product, namely MODIS collection 5 (MC5), uses a combination of 6 ice particle shape habits with smooth surfaces to retrieve cirrus cloud properties [17,18]. MC5 assumes small crystals to be compact, such as droxtals and single hexagonal columns and plates, while large crystals to be fluffy, such as bullet rosettes and hexagonal column aggregates. This assumption is consistent with the microphysical process of ice particle growth, that is, small particles grow mainly via condensation of water vapor onto the ice particle surface to form compact particles, whereas large particles grow mainly via coagulation of grown crystals to form fluffy particles. Observations also show that large ice particles tend to be fluffier

\* Corresponding author.

E-mail address: [tang2013@tamu.edu](mailto:tang2013@tamu.edu) (G. Tang).

[19,20]. However, the assumption of smooth crystal surfaces leads to unrealistic scattering properties since we do not often observe halos in a cirrus cloud, which are the optical feature of large (relative to visual solar wavelengths) ice crystals (larger than a few microns) with smooth surfaces. The latest MODIS product collection 6 (MC6) assumes particles to have a specific shape for all sizes, an aggregate of 8 hexagonal columns [17,21] with roughened surfaces. Comparisons between MC5 and MC6 are reviewed in [22], which shows improvement of the consistency between solar-band and thermal-infrared (IR)-band retrieval of cirrus cloud optical thickness from MC5 to MC6.

In addition to shape and surface roughness, inhomogeneity (e.g., inclusions of sulfate, air bubbles, and soot) may have a significant effect on ice particle optical properties [23–27]. Sulfate and soot particles injected from aircraft exhaust and wildfires can serve as nuclei in the formation of ice particles [28]. A previous laboratory study [29] of the formation of air bubbles on a freezing water-ice surface suggests that air bubbles in a liquid water layer enveloping the crystal can be included in the ice when the layer freezes. Numerical study shows that air bubble inclusions in a compact hexagonal column ice particle lead to a smaller asymmetry parameter in the visible bands when the particle size is approximately 10 times the wavelength [25]. Furthermore, other phase matrix elements are significantly affected by air bubble inclusions, with larger  $-P_{12}/P_{11}$  at scattering angles less than approximately  $120^\circ$ , and smaller  $P_{22}/P_{11}$  at scattering angles smaller than  $150^\circ$  in their case. For large particles (sizes larger than about 50 times the wavelength), air bubble inclusions smooth out the phase matrix element variations with scattering angle and decrease the asymmetry parameter [23,30]. Simulations of the polarized reflectance of cirrus clouds using a particle model with air bubble inclusions agree better with satellite observations from the POLDER sensor on board PARASOL than using a pure ice particle model with the same overall shape [23]. Additionally, inclusion of air bubbles has been shown to decrease simulated diffuse transmissivity and increase spherical reflectivity of cirrus cloud in the visible bands, suggesting a smaller asymmetry factor [24].

While these previous studies focus on the effect of either surface roughness or inhomogeneity, the present study systematically investigates a combination of the two effects on the optical properties of ice crystals, radiative transfer simulations, and remote sensing of cirrus cloud properties.

The ray tracing method has been developed to simulate the optical properties of randomly oriented particles with maximum dimension larger than a few wavelengths [31–36]. It traces incoming rays following the geometric optics approximation, and then counts the outgoing rays to obtain the scattering phase matrix, scattering cross section, and single scattering albedo. Note that the Monte Carlo approach used in some radiative transfer models [37–40] can be effectively applied to light scattering calculation based on the ray tracing technique (e.g., [36]).

Yang and Liou [41] developed the improved geometric optics method (IGOM) that uses the same ray tracing scheme to calculate the near field but considers the phase interference between rays when computing the far field from the near field. Additionally, the effect of surface roughness can be included in IGOM [42] by randomly tilting the facets of the particle surface following a scheme analogous to the sea surface roughness model of [43] following the study by Macke et al. [44] when hit by rays. Similar treatment of surface roughness has been applied to conventional ray tracing methods [11]. Note that such a treatment does not describe a real surface configuration [44], but instead an ensemble of very small tilted surface facets, which may invalidate the geometric optics approximation. An alternative treatment of surface roughness uses an ensemble of irregular geometries [45,46], which tilt facets randomly as a whole but proves to be a good approximation of the

“locally and randomly tilted” surface roughness [45]. For particles of size parameters about 20, scattering calculations using IGOM achieve better consistency with the rigorous finite difference time domain (FDTD) method than does the conventional ray tracing method, whereas the differences between two ray tracing methods are smaller for larger particles [41].

To study the simultaneous effects of surface roughness and inhomogeneity, we develop a Monte Carlo ray tracing method based on IGOM to include both of the effects. In this method, described in the next section, rays are randomly scattered by inclusions in the scattering particle, as in the conventional ray tracing methods. However, instead of fixing the mean free path of rays traveling in ice particles [23,24], the mean free path is determined by the extinction coefficient (in units  $\mu\text{m}^{-1}$ ) and volume fraction of the spherical inclusions.

While most remote sensing techniques using radiance measurements exploit the first element of the Stokes parameter, the other three elements can also be useful. For example, the elements  $Q$  and  $U$  are very sensitive to the atmospheric particle shape [47–50], deviating significantly from spherical (e.g., water droplet) to facet (e.g., ice crystal) shapes in the visible bands [51,52]. The POLDER sensor measures elements  $Q$  and  $U$  for visible wavelengths from multiple angles. These measurements are used to infer ice cloud phase, ice particle shape and degree of surface roughness [51–54]. In this study, the sensitivity of polarized reflectance to the surface roughness and air bubble inclusions is analyzed and compared with POLDER data for the MC6 particle model, which is shown to underestimate the polarized reflectance from cirrus clouds [55] with only surface roughness included.

We extend the Monte Carlo ray tracing technique reported by Macke et al. [24] to include the polarization and interference of rays during internal scattering based on IGOM, to study the effects of surface roughness and inhomogeneity. The present study focuses on a case where all the inclusions are spherical air bubbles, but more general cases could be considered using our method in a straightforward manner. We give details of the methodology in Section 2 and single scattering simulation results in Section 3. Section 4 shows the retrievals of cirrus cloud optical thickness from MODIS measurements and comparisons between the simulated and observed linear polarized reflectivity from POLDER. Section 5 summarizes the major findings of this study.

## 2. Monte Carlo ray-tracing method

The conventional ray tracing method traces the 4-element Stokes vector in conjunction with a ray [56] and does not account for the phase change of rays due to light scattering by inclusions. In IGOM, because the far field is calculated from the near field, the phase interference between rays must be accounted for. Thus, in our implementation of Monte Carlo ray tracing technique, instead of tracing the Stokes parameters the electromagnetic field itself is traced. Because we assume the rays are plane waves, the magnetic field is related to the electric field following the plane wave relation [57]:

$$\mathbf{H} = \frac{\varepsilon}{\mu} \mathbf{n} \times \mathbf{E} \quad (1)$$

where

- $\mathbf{E}$  = electric field;
- $\mathbf{H}$  = magnetic field;
- $\mathbf{n}$  = ray propagation direction vector;
- $\mu$  = permeability of the medium;
- $\varepsilon$  = permittivity of the medium.

In our Monte Carlo approach, we follow rays and determine their interactions with bubbles in iterations of a basic sequence of steps: the distance a given ray travels before encountering a bubble is chosen, the size of the bubble it encounters is chosen, and the direction in which the scattered ray travels is chosen. Each of these choices is made stochastically according to proposed probability distributions, as will be explained. Sampling from the proposed distribution is made by sampling a variable  $\xi$  a uniform [0,1] distribution and then making use of the fact that if  $P$  is the cumulative distribution function for a probability distribution  $p$  and if a variable  $y$  is determined by the relation

$$P(y) = \xi \quad (2)$$

i.e. if  $y = P^{-1}(\xi)$ , then  $y$  has the probability distribution  $p$ .

As a model for the size distribution of spherical bubbles, we use a gamma distribution model  $N(r)$  for the number of bubbles with radius  $r$  per unit volume used in [58] in another context:

$$N(r) = Cr \left( \frac{1}{v_{eff}} - 3 \right) e^{-\frac{r}{r_{eff} v_{eff}}} \quad (3)$$

Here  $N(r)dr$  is the probable number of bubbles with radii between  $r$  and  $r + dr$  occurring per unit volume, and the two key parameters  $r_{eff}$  and  $v_{eff}$  are the “effective” mean and variance of the size distribution. The number  $C$  defined by

$$C = \frac{N_0}{\left( v_{eff} r_{eff} \right) \left( \frac{1}{v_{eff}} - 2 \right) \Gamma \left( \frac{1}{v_{eff}} - 2 \right)} \quad (4)$$

is a normalizing constant, with  $N_0$  the total number of bubbles per unit volume

$$N_0 = \int_0^\infty N(r) dr \quad (5)$$

(see [58] for details). In this study,  $r_{eff}$  and  $v_{eff}$  are fixed at  $1 \mu\text{m}$  and  $0.1$ , while the influence of inclusion size is not considered but can be a future topic.

In what follows we will find it useful to refer to the normalized version  $f(r) = N(r)/N_0$ , which satisfies

$$\int_0^\infty f(r) dr = 1 \quad (6)$$

Applying the usual slab argument in which a photon beam enters a slab of infinitesimal thickness  $ds$  and cross section  $L^2$ , the probability of extinction in the distance  $ds$  is  $\kappa ds$ , where  $\kappa$  is the extinction coefficient associated with the inclusions. It is defined in terms of the extinction cross section  $C_{ext}(r)$  of a bubble of radius  $r$  by

$$\kappa = \int_0^\infty C_{ext}(r) N(r) dr \quad (7)$$

It will be useful to write  $\kappa$  in terms of the fraction  $v_f = \int_0^\infty \frac{4}{3} \pi r^3 N(r) dr$  of the total crystal volume taken up by bubbles:

$$\kappa = v_f \cdot \frac{\int_0^\infty C_{ext}(r) f(r) dr}{\int_0^\infty \frac{4}{3} \pi r^3 f(r) dr} \quad (8)$$

With probability of bubble encounter in the interval  $(l, l + dl)$  given by  $\kappa dl$ , the probability that a ray travels a total distance  $l$  before a bubble encounter is given by the exponential distribution  $p(l) = \kappa \exp(-\kappa l)$ . The mean of this distribution is  $1/\kappa$ , so the mean free path  $l_f$  and cumulative distribution function are defined by

$$l_f = \frac{1}{\kappa}$$

$$P(l) = 1 - \exp \left( -\frac{l}{l_f} \right) \quad (9)$$

According to Eqs. (8) and (9), a larger volume fraction or extinction coefficient of inclusions leads to a shorter mean free path, resulting a higher probability of encountering an inclusion.

In our Monte Carlo scheme, for a given ray we first pick the distance  $l$  that a ray travels before encountering a bubble according to the probability distribution  $p$ . We know that if  $\xi_0$  is chosen from a uniform distribution then  $l$  chosen such that  $1 - \exp \left( -\frac{l}{l_f} \right) = \xi_0$  will have the desired exponential distribution. Furthermore, since  $\xi_1 = 1 - \xi_0$  is also uniformly distributed and  $\xi_1$  then equals  $\exp \left( -\frac{l}{l_f} \right)$ , we simply choose a value for  $\xi_1$  from a uniform [0,1] distribution and then require that

$$l = -l_f \ln(\xi_1) \quad (10)$$

We assume that the radii of inclusions follow a gamma distribution with a probability distribution function  $f(r)$ . The probability that a bubble has radius  $r$  is.

$$\frac{f(r') C_{ext}(r') dr'}{\int_0^\infty f(r') C_{ext}(r') dr'}$$

Then the radius  $r$  of the encountered bubble is determined by taking  $\xi_2$  from a uniform distribution and then requiring

$$\frac{\int_0^r f(r') C_{ext}(r') dr'}{\int_0^\infty f(r') C_{ext}(r') dr'} = \xi_2 \quad (11)$$

Upon the determination of sphere radius  $r$ , the optical properties of this spherical inclusion are calculated using the Lorenz-Mie theory [59]. One should note that the standard Lorenz-Mie solution is exact only for spheres enclosed in a non-absorptive medium. For spheres enclosed in an absorptive medium, a modified Lorenz-Mie solution must be used [60–62]. A notable difference of the modified from the standard Lorenz-Mie solution is that the extinction efficiency (defined as the ratio of extinction cross section to the geometric cross section) approaches 1 rather than 2 when the radius is infinitely large, which results from the elimination of the contribution from diffraction. In this study, we focus on air bubbles included in ice particles, a nearly non-absorptive medium for visible wavelengths. Thus, the standard Lorenz-Mie solution is used. For thermal infrared wavelengths, because the specified bubble radii are much smaller than the wavelength, the extinction efficiency is small, thus the effect of bubble inclusion is neglected.

Knowing the optical properties of the encountered bubble, the ray direction after scattering by an inclusion is then sampled by a Monte Carlo scheme in two steps, first choosing the scattering angle and second choosing the azimuth angle, where the angles:

- $\theta$  = scattering angle (between the directions of incoming and scattered rays);
  - $\varphi$  = azimuth angle between the scattering plane and the defined  $l_i$  axis;
- are as illustrated in Fig. 1.

The scattering angle  $\theta$  is chosen first, and is required to satisfy

$$\frac{1}{2} \int_0^\theta P_1 \sin \theta' d\theta' = \xi_3 \quad (12)$$

where  $\xi_3$  is uniform [0,1]. Here  $P_1$  is the single scattering phase function of the bubble, normalized so that the left hand side in Eq. (12) equals 1 when  $\theta = \pi$ .

Then the azimuth angle  $\varphi$  is chosen in terms of another

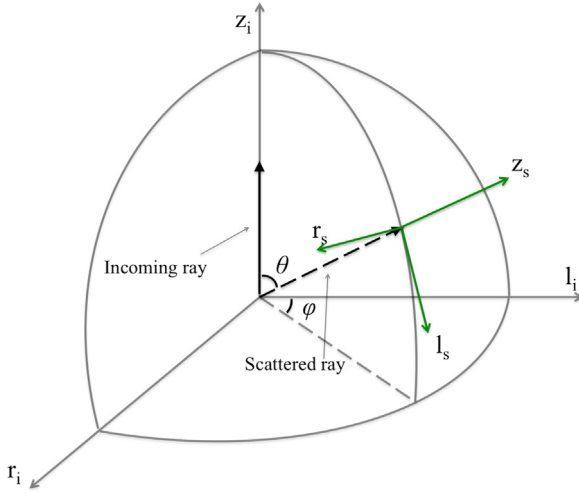


**Fig. 1.** Geometry of the incoming and scattered rays. Two sets of 3D Cartesian coordinates,  $(r_i, l_i, z_i)$  and  $(r_s, l_s, z_s)$  are illustrated. The incoming ray is along the  $z_i$  axis, whereas the scattered ray is along the  $z_s$  axis. The scattering plane is the one shared by  $z_i$  and  $z_s$  axes.  $l_s$  is in the scattering plane and  $r_s$  is perpendicular to the scattering plane.  $\theta$  is the scattering angle.  $\varphi$  is the azimuth angle. The  $(r_s, l_s, z_s)$  coordinates will work as  $(r_i, l_i, z_i)$  for the subsequent internal scattering event.

uniform  $[0,1]$  variable  $\xi_4$ :

$$2\pi\xi_4 = \varphi + A \frac{\sin(2\varphi)}{2} + B \sin^2(\varphi)$$

where

$$A = \frac{(|E_l|^2 - |E_r|^2)(|S_2|^2 - |S_l|^2)}{(|E_l|^2 + |E_r|^2)(|S_2|^2 + |S_l|^2)}$$

$$B = \frac{(E_l E_r^* + E_l^* E_r)(|S_2|^2 - |S_l|^2)}{(|E_l|^2 + |E_r|^2)(|S_2|^2 + |S_l|^2)} \quad (13)$$

and  $E_l$ ,  $E_r$  are the complex electric field (including phase information) components of the incoming ray along  $l_i$  and  $r_i$  axes, which together form a 2D Cartesian coordinate perpendicular to the ray (illustrated in Fig. 1). The star symbol \* stands for the conjugate of a complex number, and  $S_1$ ,  $S_2$  are the nonzero elements of the scattering amplitude matrix (defined in p. 34 of [56]) of the encountered spherical inclusion, as functions of  $\theta$ .

Eq. (12) is used to solve for  $\theta$ . Eq. (12) and (13) are derived by assuming that the probability distribution function is proportional to the scattering intensity (see Appendix for the derivation). Note that  $|E_l|^2 + |E_r|^2$ ,  $|E_l|^2 - |E_r|^2$  and  $E_l E_r^* + E_l^* E_r$  are the first three Stokes parameter elements,  $I$ ,  $Q$ , and  $U$ , of the incoming ray that is defined in the given  $r_i$  and  $l_i$  coordinates, respectively. As such, Eq. (13) is equivalent to Eqs. (5) and (6) in [23]. For Stokes parameter tracing, one should follow the equation in that paper. For scalar ray tracing where  $Q=U=0$  is assumed, Eq. (13) reduces to  $\varphi = 2\pi\xi_3$ , a uniform distribution. We note that what is known as the “biased sampling” scheme [63] involves a different procedure, following the uniform distribution to determine the azimuth angle and then changing the intensity of the scattered ray, but in calculations not reported here has been found to produce the same Stokes parameter distribution as our scheme.

Upon determination of the scattering direction, the electric field of the scattered ray is calculated following the scattering equation:

$$\begin{bmatrix} E_l^{sca} \\ E_r^{sca} \end{bmatrix} = \begin{bmatrix} S_2(\theta) & 0 \\ 0 & S_1(\theta) \end{bmatrix} \begin{bmatrix} \cos(\varphi) & \sin(\varphi) \\ -\sin(\varphi) & \cos(\varphi) \end{bmatrix} \begin{bmatrix} E_l \\ E_r \end{bmatrix}$$

$$\cdot \sqrt{\frac{|E_l|^2 + |E_r|^2}{|E_l \cos(\varphi) + E_r \sin(\varphi)|^2 |S_2(\theta)|^2 + |E_l \sin(\varphi) - E_r \cos(\varphi)|^2 |S_1(\theta)|^2}} \cdot \omega_0 \quad (14)$$

where  $E_l^{sca}$ ,  $E_r^{sca}$  are the complex electric field components of the scattered ray along the  $l_s$ ,  $r_s$  coordinates with  $l_s$  axis in the scattering plane and  $r_s$  axis perpendicular to the scattering plane, and  $\omega_0$  is the single scattering albedo of the encountered air bubble.

Because the inclusions are spherical air bubbles, only the two diagonal elements of the scattering matrix are nonzero, and they are functions of the scattering angle  $\theta$ . The square root term in Eq. (14) is the normalization term that ensures the scattered ray's intensity to be the same as the incoming ray when the single scattering albedo of air bubbles is 1, and to be  $\omega_0$  of the incoming ray's intensity when it is less than 1. The subsequent internal scattering takes  $E_l^{sca}$  and  $E_r^{sca}$  in  $l_s$  and  $r_s$  axes respectively as the incoming  $E_l$  and  $E_r$ , and  $(r_s, l_s, z_s)$  coordinates as  $(r_i, l_i, z_i)$  coordinates. We do not constantly rotate the coordinate to a meridian plane associated with a spatially fixed coordinate for each internal scattering. A similar approach has been used (see the second Monte Carlo – Euler Monte Carlo method in [64]). The advantage of this method is that the Stokes parameter needs to be rotated only once for each internal scattering. The scattering process repeats as long as the ray is propagating inside the particle until it leaves the particle or becomes weak enough that its intensity is negligible. We choose the minimum threshold to be sufficiently small ( $10^{-6}$  of the incident ray intensity) that further decreasing this number results in relative differences of the extinction cross section, single scattering albedo, and asymmetry parameter of less than  $10^{-3}$  for a series of test cases. Because the optical properties are finally obtained by volume integration of the electric field within the particle, we assume that further tracing of rays after reaching such threshold contributes negligible part to the optical property calculation. Finally, the electric fields of all rays along their paths are collected and projected to the spatially fixed coordinates to compute the optical properties of the particle following the procedure in part 3 of [41].

### 3. Results

We first study the effect of surface roughness on the single-scattering properties of ice particles. We use IGOM to simulate the optical properties of an MC6-shaped ice particle, which is a relatively compact aggregate of 8 hexagonal columns as illustrated in Fig. 2. The nonzero phase matrix elements [56] are shown in Fig. 2. The particle consists of pure ice (no air bubble inclusions) and has maximum dimension  $D$  (the greatest distance between two points of the particle) set at  $100 \mu\text{m}$ . The incident wavelength is  $0.86 \mu\text{m}$ , the spectral center of Band 2 of MODIS. The degree of surface roughness varies from 0.0 to 2.0, where surface roughness is defined as the mean squared surface slope,  $\sigma^2$ , or the mean square of the tangent of the tilting angle of the surface normal [15] (for example,  $\sigma^2=0, 0.03, 0.5, 1, 2$  indicate an average tilting angle of about  $0^\circ, 10^\circ, 35^\circ, 45^\circ, 55^\circ$ , respectively). The smoothing of the phase function  $P_{11}$  due to increasing degree of surface roughness is evident, including vanishing of the  $22^\circ$  and  $46^\circ$  halos and the backscattering peak, as has been reported by [11,15,55]. The smooth phase function is more realistic because halos occur less frequently in nature. The phase matrix term  $P_{12}$  is of particular interest in polarization simulation as a dominant term in the determination of the polarized reflectance when  $Q$  and  $U$  are much



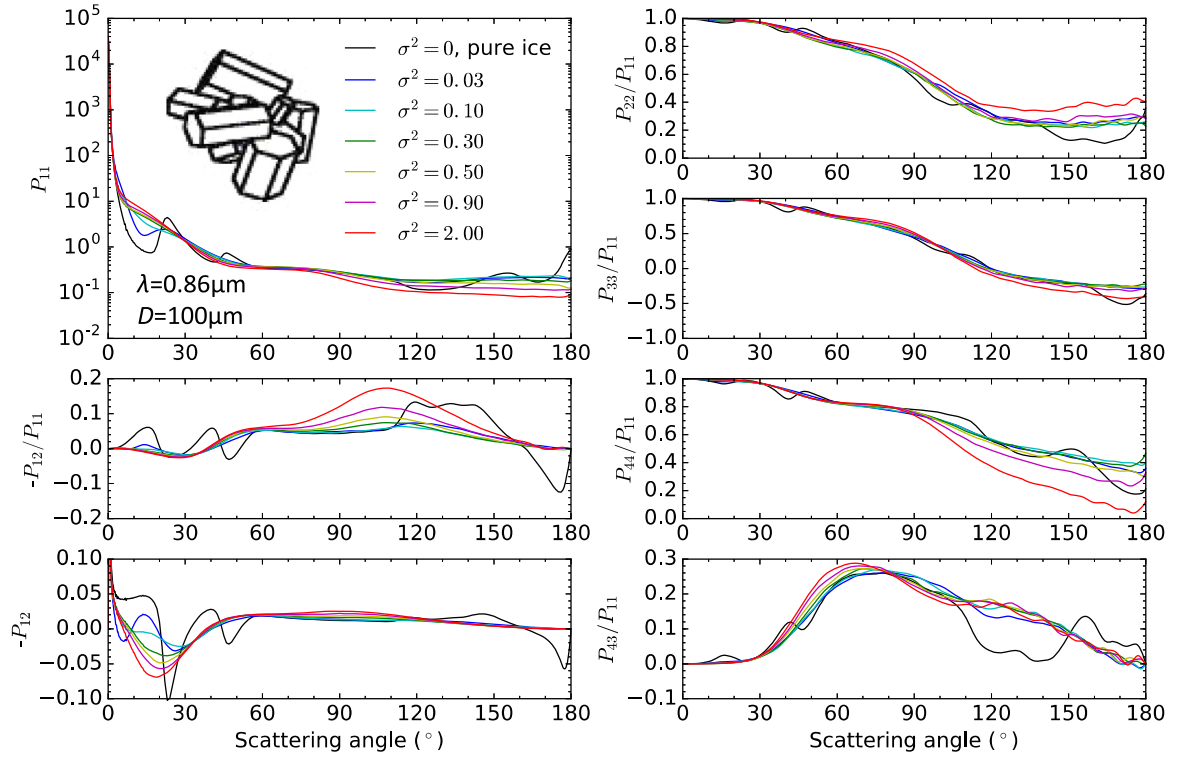


**Fig. 2.** Phase matrix elements of a randomly oriented MC6-shape cirrus cloud particle with a maximum dimension 100  $\mu\text{m}$  and varying degree of surface roughness. The incident wavelength is 0.86  $\mu\text{m}$ .

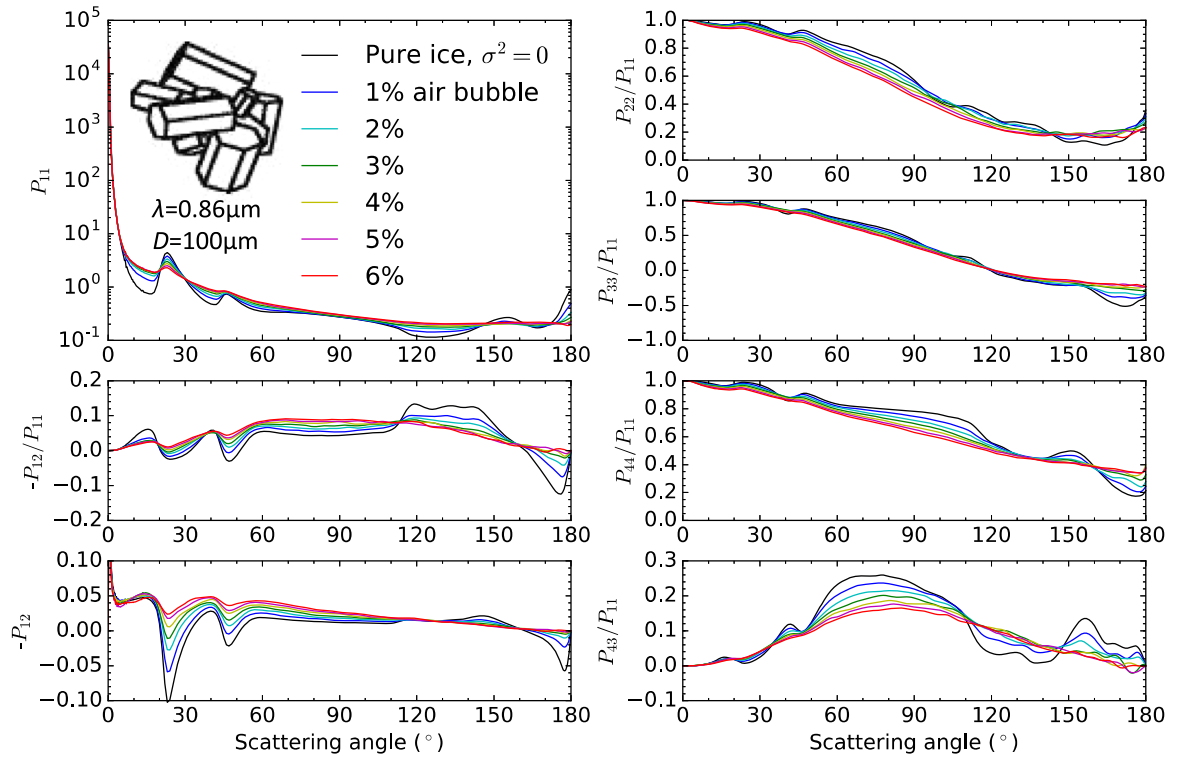


**Fig. 3.** Same as Fig. 2 but for smooth particles with a degree of surface roughness 0.0 and varying air bubble volume fraction 0 to 6%.

smaller than  $I$ , which is often the case for cloud reflectance. Although  $-P_{12}/P_{11}$  increases with  $\sigma^2$  over scattering angles between  $60^\circ$  and  $150^\circ$ , because  $P_{11}$  decreases with  $\sigma^2$  within this angle range,  $P_{12}$  is not significantly affected by surface roughness, and only increases slightly between  $60^\circ$  and  $120^\circ$ ; surface roughness

smoothes the curve outside this angle range. This presumably explains the finding by [55] that the MC6 particle model underestimates the polarized reflectance even with severe surface roughness.

To study the effect of air bubble inclusions on the single-

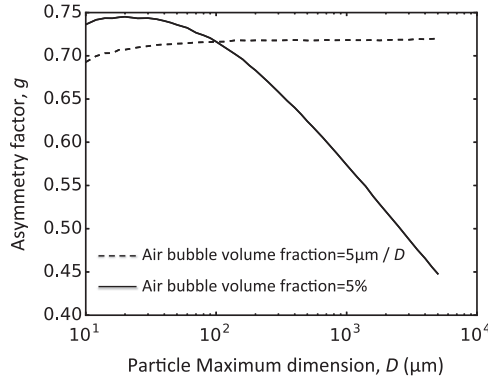


**Fig. 4.** Asymmetry parameter  $g$  as a function of the particle maximum dimension  $D$  for MC6 shape particle, smooth surfaces ( $\sigma^2=0$ ), and incident wavelength  $0.86 \mu\text{m}$ . The asymmetry parameter converges to a constant with particle size when the air bubble volume fraction times  $D$  is fixed, while it decreases monotonically with  $D$  when the air bubble volume fraction is fixed.

scattering properties of ice particles, we use our newly developed Monte Carlo IGOM to perform simulations for smooth MC6 particles with a series of air bubble volume fractions, 0%, 1%, 2%, ..., 6%. As mentioned above, the radii of the air bubbles follow a gamma distribution with an effective radius of  $1 \mu\text{m}$  and an effective variance of 0.1. The scattering properties of spherical air bubbles are calculated using the Lorenz-Mie theory [59]. The particle maximum dimension and incident wavelength are the same as in the previous simulations. The phase matrix elements are shown in Fig. 3. Similar to the effect of surface roughness, inclusion of air bubbles smoothes out the phase function, leading, for example, to the vanishing of the  $22^\circ$  and  $46^\circ$  halos and back-scattering peaks as reported by [11,23,24]. The decreases of  $P_{22}/P_{11}$ ,  $P_{33}/P_{11}$ , and  $P_{44}/P_{11}$  due to air bubble inclusions are significant, compared with the effect of surface roughness.  $-P_{12}/P_{11}$  is also affected significantly, decreasing with the bubble volume fraction between  $20^\circ$ – $110^\circ$  and  $160^\circ$ – $180^\circ$  and increasing between  $110^\circ$ – $160^\circ$ . In particular, between  $60^\circ$  and  $110^\circ$ ,  $-P_{12}$  increases much more significantly than is the case when surface roughness increases. Such a phenomenon suggests that air bubble inclusion may significantly affect the polarized reflectivity of cirrus clouds, though the physical mechanism responsible is as yet unclear.

The asymmetry parameter ( $g$ ) indicates the fraction of energy that is transmitted through the cloud, hence is an important indicator of the clouds' effect on the Earth energy balance. Larger  $g$  in visible bands indicates smaller reflection (or cloud albedo) of solar radiation by cloud, leading to a warming effect on the earth surface [65]. Measured values of  $g$  for cirrus clouds range roughly from 0.70–0.76 [66–70], although the technique in these studies is based on measurements that do not allow estimation of the part of the forward peak of the phase function due to the  $\delta$ -transmission through parallel facets [71,72]. Numerical simulations of  $g$  range more widely, from about 0.74 for polycrystals [44] to 0.85 for a solid hexagonal column shape [33]. For a fixed hexagonal column shape,  $g$  increases with size and approaches a constant when the size is much larger than the wavelength, and decreases monotonically with surface roughness or distortion [44]. Fig. 4 shows variations of the asymmetry parameter with  $D$  when air bubble inclusions are present. If we simply assume a constant air bubble volume fraction when studying the effect of air bubble inclusions on the optical properties' size variation, the asymmetry parameter monotonically decreases with  $D$ . However, if we assume that the product of the air bubble volume fraction and  $D$  ( $V_f D$ ) is constant, the asymmetry parameter approaches a constant with increasing  $D$ . This numerical phenomenon can be understood by drawing the ray paths along with the particle geometry. When  $V_f D$  is kept

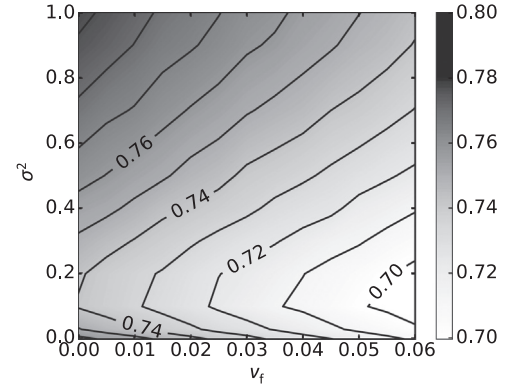


**Fig. 5.** Asymmetry parameter  $g$  of the MC6 shape ice particle as a function of bubble volume fraction  $v_f$  and degree of surface roughness  $\sigma^2$  for  $D=100 \mu\text{m}$ ,  $\lambda=0.86 \mu\text{m}$ .

constant, all figures with different particle sizes are similar. However, when the air bubble volume fraction is kept constant, the incident rays are more possibly scattered by the inclusions when the particle is larger. Because the measurements have a relatively narrow range as previously discussed, it is difficult to obtain the relation between  $g$  and size. Thus, we continue to assume that the volume fraction is constant when doing retrieval, until further evidence is found to suggest a better assumption. More investigation of factors affecting  $g$  then can be attempted here:  $g$  varies in at least a 3-dimensional parameter space composed of  $\sigma^2$ ,  $v_f$ , and size, and in fact  $g$  may well also vary with particle shape and air bubble radius.

Fig. 5 shows the asymmetry parameter as a function of  $v_f$  and  $\sigma^2$  for a fixed  $D=100 \mu\text{m}$ . The U-shape of the asymmetry parameter variation – decreasing and then increasing with  $\sigma^2$  with a minimum near  $\sigma^2=0.15$  and the monotonic decrease of the asymmetry parameter with air bubble volume fraction have been reported [23]. The U-shaped variation with  $\sigma^2$  is shape dependent. For a long hexagonal column,  $g$  decreases monotonically with degree of surface roughness [44]. While the decrease with  $\sigma^2$  can be understood by the reduction of  $\delta$ -transmission due to parallel facets, it is difficult to understand the increase of  $g$  with  $\sigma^2$ . One possible explanation is for the rays to pass through facets more easily because both reflected and refracted rays can be on the same side of the encountered facet for a severely tilted surface, and the  $\delta$ -transmission is already reduced considerably because of aggregation. Such a phenomenon exists in the numerical implementation of surface roughness but might not be natural. However, ray tracing on an explicitly roughened particle (surface facets are discretized and distorted following [43]'s scheme) also results in this phenomenon, suggesting that the increase of  $g$  with size can be natural, though such discretization may invalidate the geometric optics approximation when the small facets' length scale is not very large compared with the wavelength. Further investigation of the effect of surface roughness on  $g$  is needed. The monotonic decrease of  $g$  with  $v_f$  may be understood in terms of the intuitive argument that  $\delta$ -transmission is reduced and there is an increased possibility of scattering of forward propagating rays by air bubbles.

#### 4. Satellite retrieval and polarimetric simulation

As discussed in the introduction, the optical properties of cirrus cloud particles are sensitive to particle shape and size, and also orientation, especially for lidar retrieval. This makes it difficult to accurately retrieve cirrus cloud properties from satellite solar band

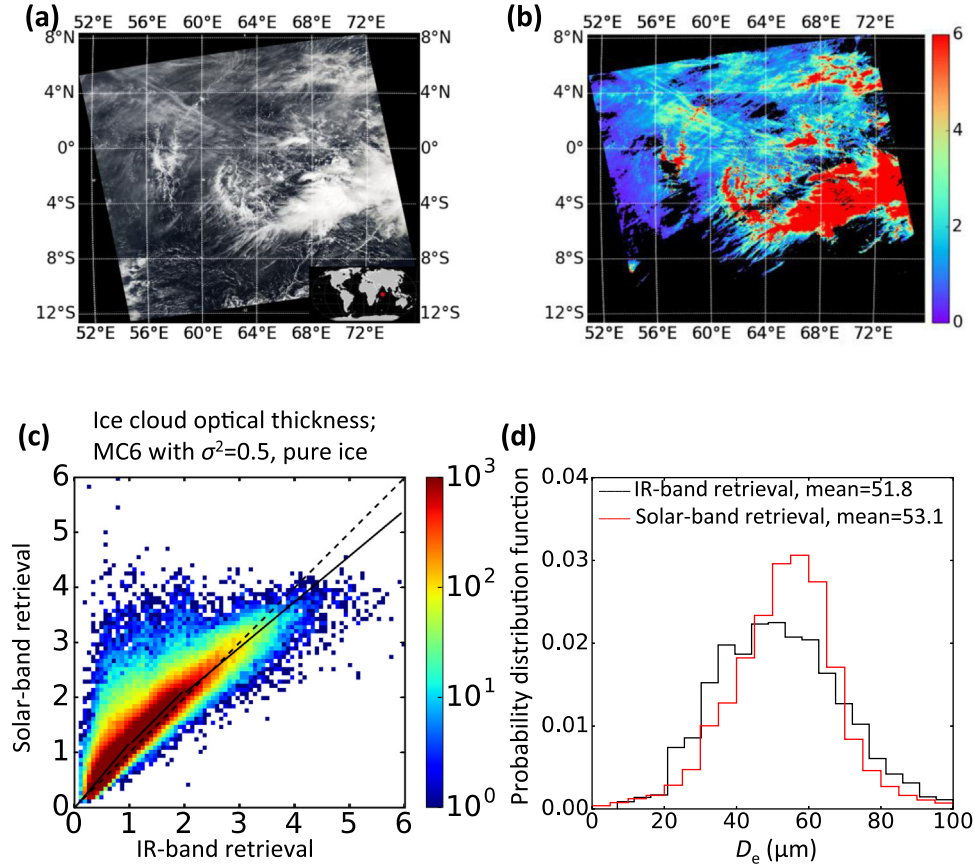


**Fig. 6.** (a)MODIS (on Aqua) granule from 0920 UTC: 22JUL2006; (b) Solar band retrieval of cirrus cloud optical thickness using the standard MC6 particle model; (c) Observational density of cirrus cloud optical thicknesses from IR-band and solar-band retrievals, where the three solid lines represent the least square fits in the ranges of IR-band retrieval between 0–1, 1–2, and 2–6; (d) probability distribution functions of the IR-band retrieved  $D_e$  and solar-band retrieved  $D_e$ .

observations. The retrieval of cirrus cloud optical thickness using IR band observations is generally supposed to be more accurate because cirrus cloud particle optical properties are relatively insensitive to the particle shape in these bands [73,74,22]. Therefore, when retrieving simultaneously the cirrus cloud particle size and optical thickness by assuming a fixed particle shape, using the IR bands presumably gives more accurate results than using the solar bands. However, IR-band retrieval is limited to thin ice cloud because the sensitivity decreases significantly with optical thickness when the thickness exceeds about 6 [73], while solar-band retrieval is sensitive up to optical thickness of about 30 [75]. Thus both bands are needed to accurately retrieve cirrus cloud optical thickness. To test the self consistency of a particle model, we can compare solar- and IR-band retrievals within the range of optical thickness 0–6. In this study, we perform the retrieval using both IR and solar bands assuming an MC6 particle model, with addition of varying degrees of surface roughness and air bubble volume fractions. For a case study we choose a granule taken by MODIS on board Aqua at 0920 UTC 22 July 2006 (Fig. 6a) located over the tropical Indian Ocean. For the solar-band retrieval we employ the Nakajima-King scheme [75] using the  $0.86\ \mu\text{m}$  (band-2) and  $2.13\ \mu\text{m}$  (band-7) band radiance measurement, and for the IR-band retrieval we employ the split-window scheme [76,77] using the  $11\ \mu\text{m}$  (band-31) and  $12\ \mu\text{m}$  (band-32) band radiance measurement. For the solar band retrieval we first build a 5-dimensional look-up table, in the parameter space of solar zenith angle, viewing zenith angle, relative azimuth angle, cirrus cloud optical thickness, and effective diameter. For a given pixel, a two dimensional “sub-look-up-table” is obtained by interpolation over three angular dimensions. Then we employ a Levenberg-Marquardt

scheme to retrieve the cirrus cloud optical thickness and effective diameter simultaneously. The Levenberg-Marquardt scheme is a kind of damped least square scheme and converges globally rather than locally (ad does, for example, the Gauss-Newton scheme), so it is more robust than the latter. Moreover, the effect of simulation and measurement errors on the retrieval result can be included in the scheme. In this study, for simplicity, we do not consider the effect of these errors.

Fig. 6b shows the solar-band retrieval of  $\tau$  using the standard MC6 particle model (i.e. pure ice, and  $\sigma^2=0.5$ ). Figs. 6c and d show the comparison between the solar-band retrieval and IR-band retrieval of  $\tau$  and  $D_e$ . The granule has 1918108 cirrus cloud pixels (from MODIS level 2 product). Using the standard MC6 particle model, we obtain good agreement between the solar-band and IR-band retrievals, as also reported by [22]. In the case study, the solar-band retrieval tends to result in a slightly larger effective size with a narrower distribution than the IR-band retrieval. More case studies should be carried out to gain a statistically robust conclusion. Note in Fig. 6c that there are quite a few pixels with IR-band retrieved  $\tau$  about 0–2 and solar-band retrieved  $\tau$  about 2–4. The overestimated  $\tau$  from solar-band retrievals could result from falsely recognizing lower cloud or multi-layer cloud as cirrus cloud. Also adjacent pixels can affect the retrieval through a 3D effect, which is not accounted for in our 1D retrieval. Ideally, one can define an index to quantify the self consistency, e.g., as the relative difference of the mean value between two band retrievals, or the slope of a least square fit. However, in this case study, the “noise” areas may contaminate the index, and it is difficult to eliminate them. Thus we only discuss the self consistency qualitatively. Fig. 7 shows comparisons of solar-band and IR-band



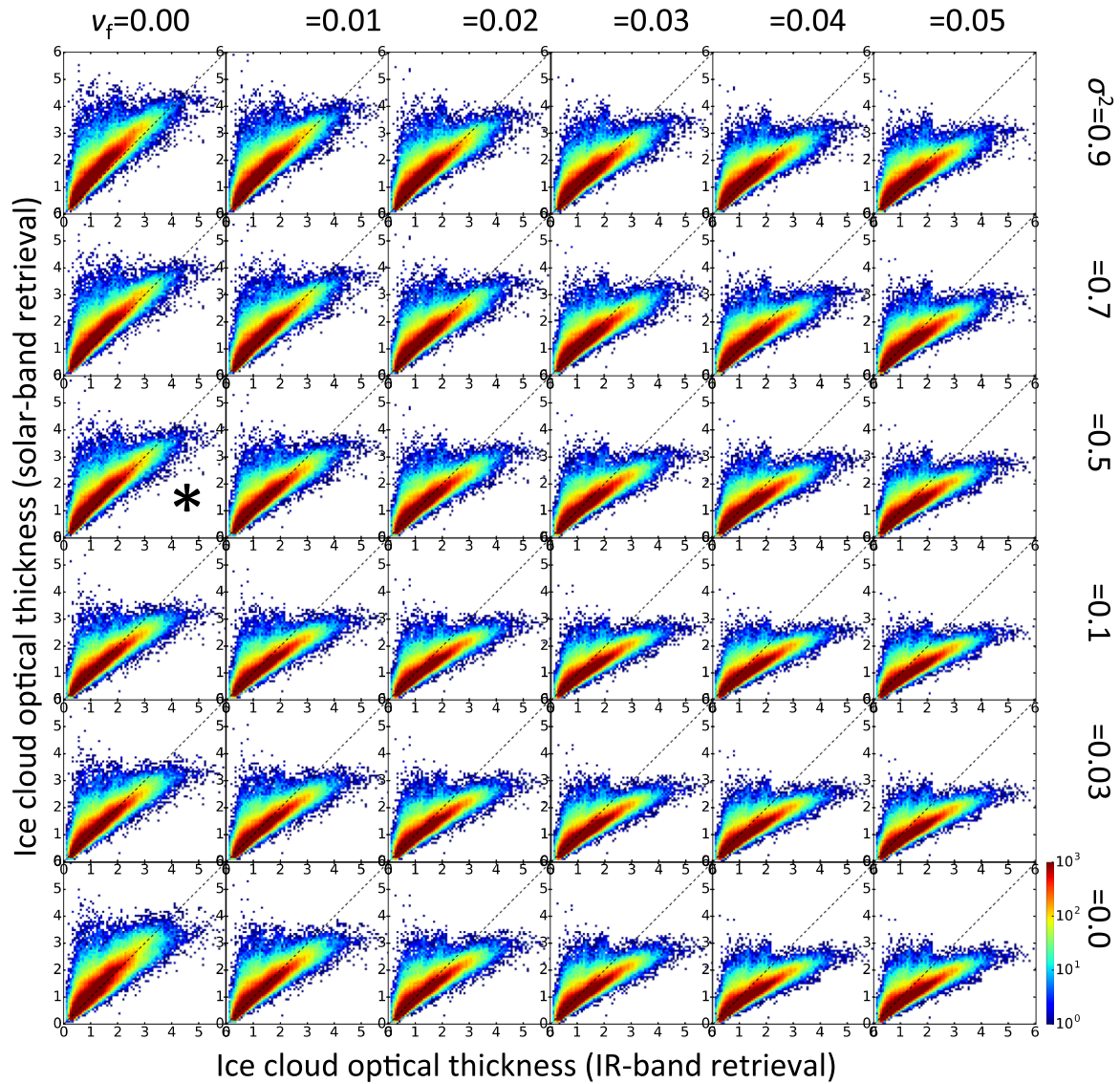


**Fig. 7.** Observational density of solar-band retrieved cirrus cloud optical thickness for varying  $\sigma^2$  and  $v_f$  vs. IR-band retrieval for the granule in Fig. 6. The standard MC6 case is a replication of Fig. 6c, indicated by panel with \* sign. The columns are for  $v_f=0, 0.01, 0.02, 0.03, 0.04, 0.05$  from left to right, and the rows are for  $\sigma^2=0.0, 0.03, 0.1, 0.5, 0.7, 0.9$  from bottom to top. The scales of the x-axis and y-axis are optical thickness 0–6 for each plot.

retrievals of  $\tau$ , when using various  $\sigma^2$  and  $v_f$  values in the MC6 particle model. Overall from the figure, a higher  $v_f$  leads to smaller solar-band  $\tau$  retrievals. The ( $\sigma^2=0$ ,  $v_f=0$ ) case achieves relatively good self consistency, while the solar-band retrieval tends to decrease from  $\sigma^2=0$  to  $\sigma^2\approx 0.1$  and then increase to achieve good self consistency when  $\sigma^2=0.5$ . Further increasing  $\sigma^2$  leads to larger solar-band retrievals, reducing self consistency. Notice that the variation of IR-band retrieved  $\tau$  with various  $\sigma^2$  and  $v_f$  is negligible, presumably according to the insensitivity of scattering properties to particle shape in the IR bands. Solar-band retrievals of  $\tau$  strongly depend on  $g$  of ice particles. Qualitatively, greater  $g$  implies greater cloud transmission and smaller reflectance, leading to greater  $\tau$  retrievals. The  $g$  pattern shown in Fig. 5 can help to explain the variation of solar-band retrievals of  $\tau$  shown in Fig. 7. With increasing  $v_f$ ,  $g$  decreases, then the cloud reflection increases, therefore the solar-band retrieval of  $\tau$  decreases. Similarly, with increasing  $\sigma^2$ ,  $g$  decreases and then increases, so retrieved  $\tau$  also decreases and increases.

The satellite polarized radiance measurements provide additional information beyond that provided by the unpolarized

radiance. For example, the linear polarized reflectivity measurement can be used to distinguish cloud phases, because the phase matrix element  $P_{12}$  of water cloud droplets and cirrus cloud crystals is very different [40,51,52]. The linear polarized reflectivity [23] of cirrus clouds in the visible bands is so sensitive to the degree of surface roughness and shape of cirrus cloud particles that these two parameters are retrieved from multi-angle polarization radiance measurements by the POLDER sensor on board the PARASOL satellite [53,54].

In this study, we perform forward RTM simulations in order to study the effects of surface roughness and air bubble inclusions on the polarized reflectivity. Fig. 8 shows the forward simulated normalized modified polarized radiance ( $L_{\text{nmp}}$ , defined in [23]) using the MC6 particle shape model with various  $\sigma^2$  along with the observations. For simulations, the assumed cirrus cloud optical thickness and ice particle effective diameter are 5 and 50  $\mu\text{m}$ , respectively. An optical thickness of 5 is assumed to be thick enough for the simulated  $L_{\text{nmp}}$  to be approximately a constant since  $\sigma^2 > 5$  results in very little change of  $L_{\text{nmp}}$  [53] and there is very little surface contamination. At the moment, we focus on the effects of surface roughness and air bubble inclusions, so the effective

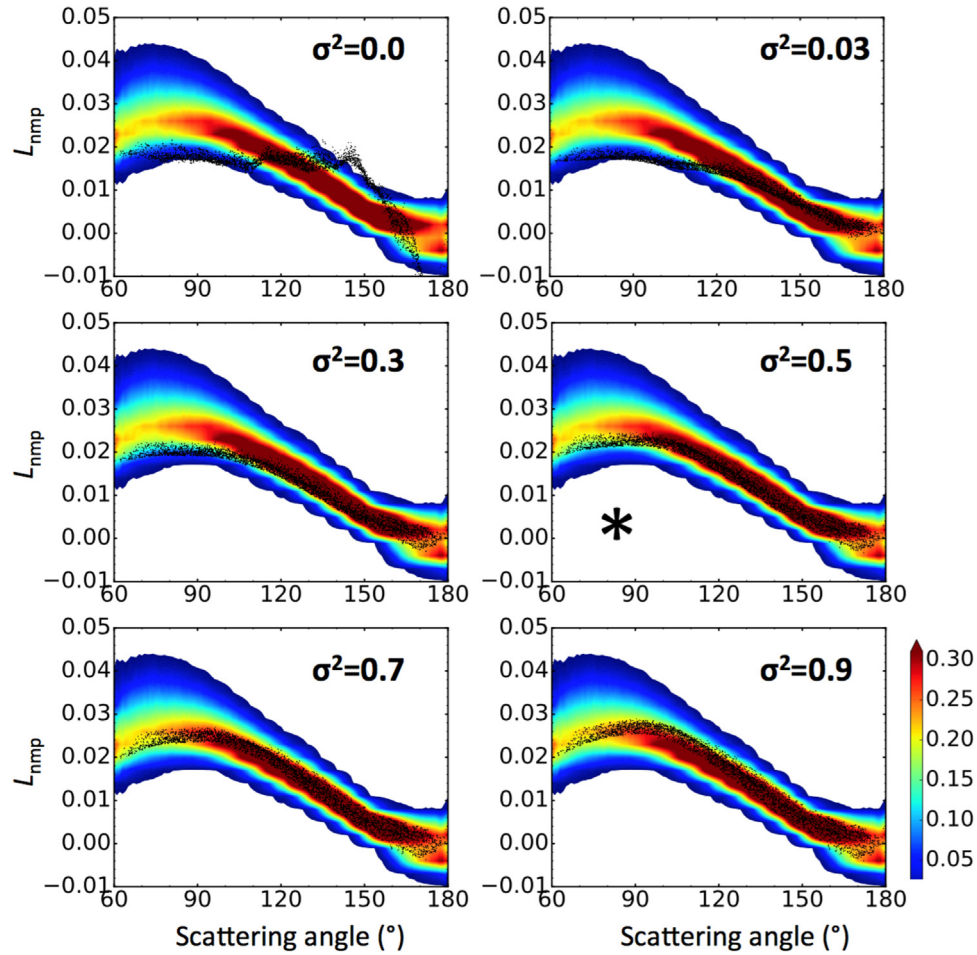


**Fig. 8.** Observational density of  $L_{nmp}$  in the  $0.865 \mu\text{m}$  band from the POLDER sensor on board PARASOL during SEP2006. Each plot is based on 4043219 pixels. (Dots): Forward RTM simulated  $L_{nmp}$  using the same solar and viewing geometries as the observations and the same cloud top height in the level 2b data. In the simulations the cirrus cloud optical thickness and effective diameter are assumed to be 5 and  $50 \mu\text{m}$ , respectively. The cirrus cloud particles are assumed to have the MC6 shape with various  $\sigma^2$  (specified at the upper right corner of each panel) and  $v_f = 0.0$ . The standard MC6 simulation is the middle right panel, indicated by a \* sign.

diameter of ice particles is fixed at  $50 \mu\text{m}$ , which is about the most probable value for cirrus clouds indicated in Fig. 6d. Three cloud top height values, 8 km, 9 km, and 10 km, are used in the simulations, for future interpolation using observed cloud top height.

The observational data is taken in September 2006 and is filtered using the criteria shown in Table 1. High confidence in the level 2b data for ice cloud pixels is achieved when all three schemes to retrieve cloud phase infer ice cloud pixels [78]. The pixels with sunglint (the angle between the satellite viewing direction and direct solar reflection from the ocean surface is smaller than  $30^\circ$ ) are not used, because direct surface reflection can contaminate the reflection from clouds, even when clouds are thick. To reduce 3D effect due to contamination from adjacent pixels,  $3 \times 3$  super pixels are used instead of single pixels, and the observational data,  $I$ ,  $Q$ , and  $U$ , are averaged over 9 pixels. To reduce

sub-pixel effects, we select super pixels whose 9 pixels are all cirrus clouds with high confidence and with 100% cloud fraction. Pixels with optical thickness larger than 5 are used for the same reasons as in simulations. Pixels with cloud top height 8–10 km are used, which is the typical cloud top height range for cirrus clouds, though its variation with latitude is neglected. We use the adding-doubling model to do the RTM simulations for solar zenith angles from  $0^\circ$ – $85^\circ$ , viewing zenith angles from  $0^\circ$ – $85^\circ$ , and azimuth angles from  $0^\circ$ – $180^\circ$  with ingredient of  $5^\circ$ , and for cloud top height 8–10 km with an increment of 1 km. The simulations are then interpolated into each observational solar zenith angle, viewing zenith angle, azimuth angle, and cloud top height for comparison. Using the standard MC6 particle shape model ( $\sigma^2 = 0.5$ , pure ice), the simulations agree with the observations well for scattering angles from  $110^\circ$ – $180^\circ$  while underestimating them from  $60^\circ$ – $110^\circ$ . In  $60^\circ$ – $110^\circ$ , with smaller  $\sigma^2$  the simulations tend to further underestimate the linear polarization reflectivity, but with larger  $\sigma^2$ , the reflectivity is overestimated in  $110^\circ$ – $140^\circ$ .

The effect of air bubble inclusions on the linear polarized reflectivity simulations can be seen in Fig. 9. With air bubble inclusions  $L_{nmp}$  tends to be overestimated in the scattering angle range of  $60^\circ$ – $110^\circ$ . For larger scattering angles, simulations with air bubble inclusions tend to agree better with the observations, but not as well as the simulations with  $\sigma^2 > 0.5$  in Fig. 8.

In order to quantify the effect of surface roughness and air bubble inclusions on the linear polarization simulations, we define

**Table 1**

Filtering criteria of the PARASOL data taken in September 2006.

Cell size	Super cell ( $3 \times 3$ pixels, or $18 \times 18 \text{ km}$ )
Band	$0.865 \mu\text{m}$
Cloud fraction	= 100%
Land/sea	Sea
Cloud optical thickness	> 5
Cloud phase	Cirrus cloud with high confidence
Cloud top height	8–10 km
Sun glint angle	> $30^\circ$

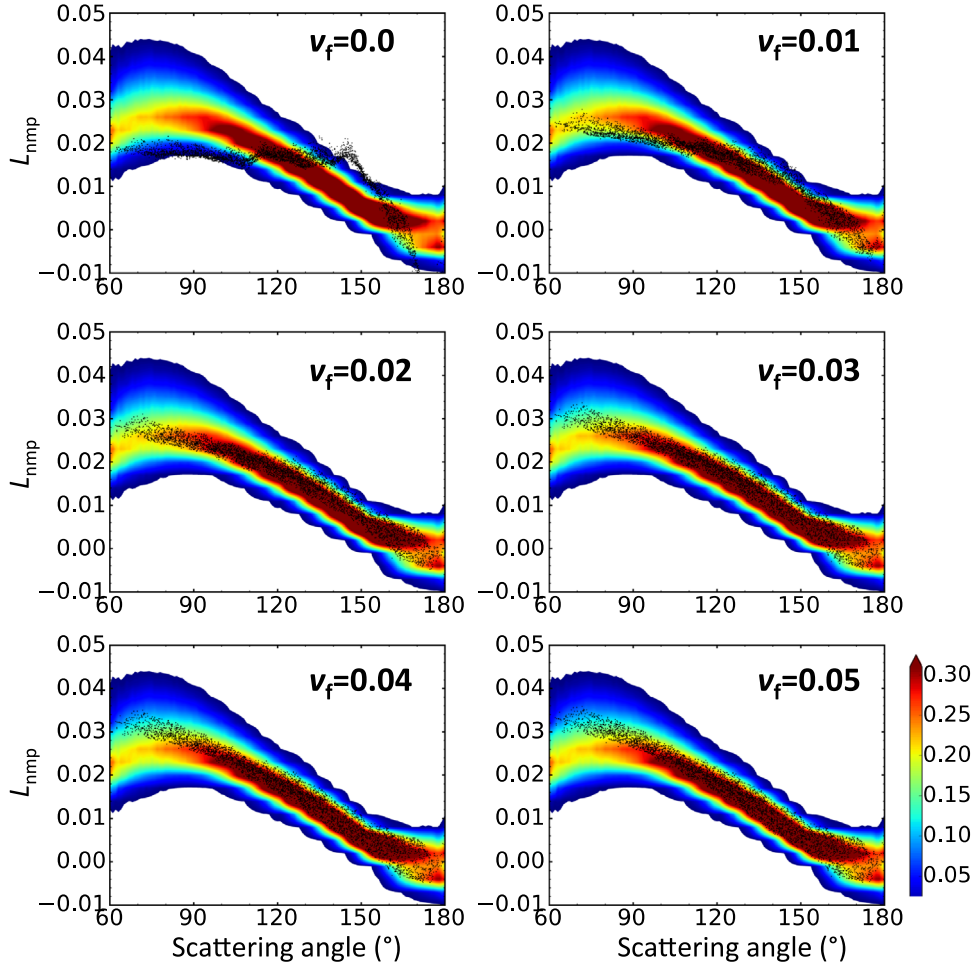


Fig. 9. Same as Fig. 8 but for various  $v_f$  and  $\sigma^2=0$ . The standard MC6 simulation is not shown.

a nonnegative parameter measuring the difference between the simulated results and the corresponding observations as:

$$\Delta = \left( \frac{\sum_{\theta=60^\circ}^{179^\circ} \left[ y_{sim}(\theta-\theta+1^\circ) - y_{obs}(\theta-\theta+1^\circ) \right]^2}{\sum_{\theta=60^\circ}^{179^\circ} \left[ y_{obs}(\theta-\theta+1^\circ) \right]^2} \right)^{\frac{1}{2}} \quad (15)$$

where  $\theta$  is the scattering angle, and  $y_{obs}$  and  $y_{sim}$  are the observed and simulated  $L_{nmp}$ . The term  $\left[ y_{sim}(\theta-\theta+1^\circ) - y_{obs}(\theta-\theta+1^\circ) \right]^2$  represents the mean squared difference between simulation and observation occurring between scattering angles  $\theta$  and  $\theta+1^\circ$ . A contour plot of  $\Delta$  as a function of  $\sigma^2$  and  $v_f$  is shown in Fig. 10, for two effective particle sizes. Along both axes, the variation of  $\Delta$  forms a U shape:  $\Delta$  reaches a minimum at about  $\sigma^2=0.9$  along the  $\sigma^2$  axis, which is consistent with the retrieval of degree of surface roughness in [54]. The variation of  $\Delta$  along the  $v_f$  axis depends on size. The minimum  $\Delta$  appears at smaller  $v_f$  when size increases because the effect of air bubble inclusion is larger. It appears that polarimetric simulation using the MC6 particle model could be improved by including both surface roughness and air bubble inclusions. While  $\Delta$  takes into account all scattering angles equally, smaller scattering angle pixels are weighted more than larger angle ones because the former are fewer than the latter. For these smaller angle observations, both the solar zenith angle and viewing zenith angle are large, so the 3D effect (e.g., the horizontal effect from adjacent pixels and the vertical effect from lower atmosphere and surface) can be large. Moreover, Rayleigh scattering, which is highly polarized, of the atmosphere above the cirrus cloud can be another error source for small scattering angle pixels,

considering that the cloud top height is not perfectly measured and there is sub-pixel variation.

## 5. Discussion and conclusion

The effects of surface roughness and air bubble inclusions on the optical properties of cirrus cloud ice particles are studied. Using IGOM, surface roughness is simulated by randomly tilting the local surface encountered by each incident ray [79]. We add a Monte Carlo ray tracing scheme to IGOM to simulate the effect of air bubble inclusions. The simulation results show that both surface roughness and inhomogeneity play a role in smoothing the phase function, with the former more effective than the latter. However, they have different effects on the phase matrix element  $-P_{12}$ . Inclusion of air bubbles significantly increases  $-P_{12}$  for scattering angles from  $20^\circ$ – $110^\circ$ , while the surface roughness has similar but less effect in the range  $60^\circ$ – $120^\circ$ . The asymmetry parameter in the visible bands is significantly affected by two factors. It decreases and then increases with surface roughness, giving plots that have a U shape, and monotonically decreases as the volume fraction of air bubble inclusions increases. The U shape variation with surface roughness is shape dependent. For a simple hexagonal column particle, the asymmetry parameter decreases monotonically with surface roughness. The most likely reason is that the ray can pass through severely roughened particle surfaces more easily, and the  $\delta$ -transmission due to parallel surfaces is already reduced by aggregation. The asymmetry parameter also



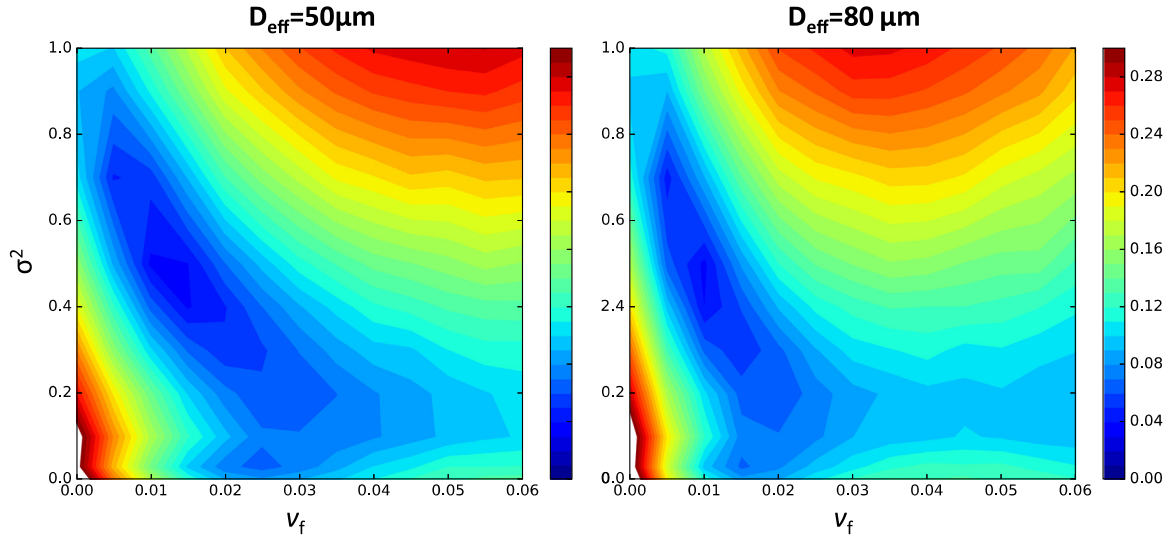


Fig. 10. Relative difference between the simulations and observations of  $L_{nmp} \Delta$  for  $D_{eff}=60 \mu m$  (left) and  $D_{eff}=80 \mu m$  (right).

decreases monotonically with particle size when the air bubble volume fraction is fixed, because rays travel greater distances in larger particles and have more chance to be scattered by inclusions.

The difference between the solar-band and IR-band retrieved cirrus cloud optical thickness follows a pattern similar to the asymmetry parameter. Presumably the asymmetry parameter of cirrus cloud particles is a good indicator for the solar-band cirrus cloud optical thickness retrieval because it quantifies the fraction of transmitted and reflected solar radiation. The standard MC6 particle model achieves a good self consistency (as seen by the agreement between IR- and solar- band retrievals). Further increasing surface roughness results in greater solar-band retrieved cirrus cloud optical thickness than IR-band. However, increasing the air bubble volume fraction results in smaller solar-band retrieved optical thickness than the IR-band, which could compensate for the effect of increasing surface roughness.

The surface roughness and air bubble inclusions also have significant effects on the simulation of linear polarized reflectivity. The comparison between simulations and PARASOL satellite observations shows that using only surface roughness tends to underestimate the linear polarized reflectivity in the range of  $60^\circ$ – $110^\circ$  scattering angles. Over all angles, the agreement between simulations and observations improves with degree of surface roughness up to about  $\sigma^2=0.9$ , which is consistent with a previous study using EOF analysis [54]. Air bubble inclusions tend to overestimate the linear polarized reflectivity in the range of  $60^\circ$ – $110^\circ$  of scattering angles. The combined effects of both factors on the linear polarized reflectivity simulations are consistent with their effects on  $-P_{12}$ . The difference between simulations and observations is minimized when both effects are included. In these simulations the particle size influences the effect of air bubble inclusions more than the surface roughness, because the optical properties change more with the former than with the latter, air bubble effects on optical properties have appeared to be more sensitive to bubble size than are roughness effects.

While this study focuses on the effects of surface roughness and air bubble inclusions, it should also be noted that particle shape is also an important factor that significantly affects the ice particle optical properties [50], although with very strong surface roughness, the effect of shape may lose its significance. The minimized difference between observed and simulated polarized reflectivity and between solar- and IR- band retrieved cirrus cloud

optical thickness may also be achieved using a well configured ice particle shape habit even if no inhomogeneity is present. However, one advantage of including air bubbles in particle models is that the necessity of configuring very complicated particle shapes to match simulations and observations, with attendant concerns about uniqueness of shape for a given level of agreement, can be avoided. And more importantly, the surface roughness and inhomogeneity do exist in nature. Including the effects of them brings us closer to the physical properties of real ice crystals.

The possibility must be recognized that our results concerning effects on optical properties of air bubble inclusions are sensitive to our assumption that the air bubble size distribution follows a gamma distribution with an effective radius  $1 \mu m$  and an effective variance 0.1. Examination of the nature of this sensitivity is a topic for future investigation.

## Acknowledgements

This study was supported by the National Science Foundation (AGS-1338440). The authors thank Yifeng Ding for performing the infrared-band based retrieval.

## Appendix A : Scattering direction sampling

We explain here the result used in Eq. (12) and (13).

In an internal scattering event the electric field of the scattering ray is a function of  $\theta$  and  $\varphi$ :

$$\begin{bmatrix} E_i^{sca}(\theta, \varphi) \\ E_r^{sca}(\theta, \varphi) \end{bmatrix} \propto \begin{bmatrix} S_2(\theta) & 0 \\ 0 & S_1(\theta) \end{bmatrix} \begin{bmatrix} \cos(\varphi) & \sin(\varphi) \\ -\sin(\varphi) & \cos(\varphi) \end{bmatrix} \begin{bmatrix} E_l \\ E_r \end{bmatrix} \quad (A1)$$

where  $S_1$  and  $S_2$  are the two nonzero elements of the scattering matrix for a spherical particle;  $E_l$  and  $E_r$  are the incident electric field along  $l_i$  and  $r_i$  axes respectively;  $E_l^{sca}$  and  $E_r^{sca}$  are the scattering electric field along  $l_s$  and  $r_s$  axes respectively (See Fig. 1). Then the intensity of the scattering field is:



$$\begin{aligned}
I(\theta, \varphi) &\propto |E_i^{sca}(\theta, \varphi)|^2 + |E_r^{sca}(\theta, \varphi)|^2 \\
&= |E_i \cos(\varphi) + E_r \sin(\varphi)|^2 |S_2(\theta)|^2 \\
&\quad + |E_i \sin(\varphi) - E_r \cos(\varphi)|^2 |S_1(\theta)|^2 \\
&= \frac{1}{2} \left\{ \left( |S_2(\theta)|^2 + |S_1(\theta)|^2 \right) (|E_i|^2 + |E_r|^2) \right. \\
&\quad \left. + \left( |S_2(\theta)|^2 - |S_1(\theta)|^2 \right) \right. \\
&\quad \left. \left[ \left( |E_i|^2 - |E_r|^2 \right) \cos(2\varphi) + (E_i E_r^* + E_r^* E_i) \sin(2\varphi) \right] \right\} \\
&= \frac{1}{2} \left( |S_2(\theta)|^2 + |S_1(\theta)|^2 \right) (|E_i|^2 + |E_r|^2) \\
&\quad \left[ 1 + A \cos(2\varphi) + B \sin(2\varphi) \right]
\end{aligned} \tag{A2}$$

where  $A$  and  $B$  have the same meaning as in Eq. (13). In the Monte Carlo scheme, to sample  $\theta$  and  $\varphi$ , we assume that the probability distribution function is proportional to the scattering intensity  $I(\theta, \varphi)$ . For the 2-dimensional sampling, we first sample  $\theta$  following the relation:

$$\frac{\int_0^\theta d\theta' \int_0^{2\pi} I(\theta', \varphi) d\varphi}{\int_0^{2\pi} d\theta' \int_0^{2\pi} I(\theta', \varphi) d\varphi} = \xi_3 \tag{A3}$$

Inserting Eq. (A2) into Eq. (A3) results in Eq. (12). After sampling  $\theta$ , we next sample  $\varphi$  following the relation:

$$\frac{\int_0^\varphi I(\theta, \varphi') d\varphi'}{\int_0^{2\pi} I(\theta, \varphi') d\varphi'} = \xi_4 \tag{A4}$$

Inserting Eq. (A2) into Eq. (A4) results in Eq. (13).

## References

- [1] Myhre G, Shindell D, Bréon FM, Collins W, Fuglestad J, Huang J, Koch D, Lamarque JF, Lee D, Mendoza B, et al. Anthropogenic and natural radiative forcing. *Clim Change* 2013;423.
- [2] Ahmad E, Hartmann D. Cloud-radiative forcing and climate: results from the Earth Radiation Budget Experiment. *Science* 1989;243(4887):57–63.
- [3] Liou KN, Yang P. Light scattering by ice crystals: fundamentals and applications. Cambridge University Press; 2016.
- [4] Heymsfield AJ. Cirrus uncinus generating cells and the evolution of cirriform clouds. Part I: aircraft observations of the growth of the ice phase. *J Atmos Sci* 1975;32:799–808.
- [5] Heymsfield AJ, Miller KM, Spinhrne JD. FIRE IFO cirrus case study: cloud microstructure. [The 27–28 October 1986]. *Mon Weather Rev* 1990;118(11):2313–2328.
- [6] Pruppacher HR, Klett JD, Wang PK. Microphysics of clouds and precipitation. *Aerosol Sci Technol* 1998;28(4):381–382.
- [7] Wendling P, Wendling R, Weickmann HK. Scattering of solar radiation by hexagonal ice crystals. *Appl Opt* 1979;18(15):2663–2671.
- [8] Wendisch M, Pilewskie P, Pommier J, Howard S, Yang P, Heymsfield AJ, Schmitt CG, Baumgardner D, Mayer B. Impact of cirrus crystal shape on solar spectral irradiance: a case study for subtropical cirrus. *J Geophys Res* 2005;110:D03202.
- [9] Yang P, Wei H, Kattawar GW, Hu YX, Winker DM, Hostetler CA, Baum BA. Sensitivity of the backscattering Mueller matrix to particle shape and thermodynamic phase. *Appl Opt* 2003;42(21):4389–4395.
- [10] Sun W, Loeb NG, Yang P. On the retrieval of ice cloud particle shapes from POLDER measurements. *J Quant Spectrosc Radiat Transf* 2006;101(3):435–447.
- [11] Hess M, Koelemeijer RB, Stammes P. Scattering matrices of imperfect hexagonal ice crystals. *J Quant Spectrosc Radiat Transf* 1998;60(3):301–308.
- [12] Knap WH, Hess M, Stammes P, Koelemeijer RB, Watts PD. Cirrus optical thickness and crystal size retrieval from ATSR-2 data using phase functions of imperfect hexagonal ice crystals. *J Geophys Res* 1999;104(24):31721–31730.
- [13] Li C, Kattawar GW, Yang P. Effects of surface roughness on light scattering by small particles. *J Quant Spectrosc Radiat Transf* 2004;89:123–131.
- [14] Yang P, Kattawar GW, Hong G, Minnis P, Hu Y. Uncertainties associated with the surface texture of ice particles in satellite-based retrieval of cirrus clouds—Part I: single-scattering properties of ice crystals with surface roughness. *IEEE Trans Geosci Remote Sens* 2008;46(7):1940–1947.
- [15] Yang P, Hong G, Kattawar GW, Minnis P, Hu Y. Uncertainties associated with the surface texture of ice particles in satellite-based retrieval of cirrus clouds: part II—Effect of particle surface roughness on retrieved cloud optical thickness and effective particle size. *IEEE Trans Geosci Remote Sens* 2008;46(7):1948–1957.
- [16] King MD, Menzel WP, Kaufman YJ, Tanré D, Gao BC, Platnick S, Ackerman SA, Remer LA, Pincus R, Hubanks PA. Cloud and aerosol properties, precipitable water, and profiles of temperature and water vapor from MODIS. *IEEE Trans. Geosci Remote Sens* 2003;41(2):442–458.
- [17] Baum BA, Yang P, Heymsfield AJ, Platnick S, King MD, Hu YX, Bedka ST. Bulk scattering properties for the remote sensing of ice clouds. Part II: narrowband models. *J Appl Meteor* 2005;44(12):1896–1911.
- [18] Yang P, Zhang L, Hong G, Nasiri SL, Baum BA, Huang HL, King MD, Platnick S. Differences between collection 4 and 5 MODIS ice cloud optical/microphysical products and their impact on radiative forcing simulations. *IEEE Trans Geosci Remote Sens* 2007;45(9):2886–2899.
- [19] Heymsfield AJ, Schmitt CG, Bansemer A, Baumgardner D, Weinstock EM, Smith JT, Sayres D. Effective ice particle densities for cold anvil cirrus. *Geophys Res Lett* 2004;31:2.
- [20] Heymsfield AJ, Bansemer A, Schmitt C, Twohy C, Poellot MR. Effective ice particle densities derived from aircraft data. *J Atmos Sci* 2004;61(9):982–1003.
- [21] Platnick S, Meyer KG, King MD, Wind G, Amarasinghe N, Marchant B, Arnold GT, Zhang Z, Hubanks PA, Holz RE, et al. The MODIS Cloud Optical and Microphysical Products: collection 6 Updates and Examples From Terra and Aqua. *IEEE Trans Geosci Remote Sens* 2016;55:502–525.
- [22] Holz RE, Platnick S, Meyer K, Vaughan M, Heidinger A, Yang P, Wind G, Dutcher S, Ackerman S, Amarasinghe N, et al. Resolving ice cloud optical thickness biases between CALIOP and MODIS using infrared retrievals. *Atmos Chem Phys Discuss* 2016;16(8):5075–5090.
- [23] C-Labonnote L, Brogniez G, Buriez JC, Doutriaux-Boucher M, Gayet JF, Macke A. Polarized light scattering by inhomogeneous hexagonal monocrystals: validation with ADEOS-POLDER measurements. *J Geophys Res* 2001;106(D11):12139–12153.
- [24] Macke A, Mishchenko MI, Cairns B. The influence of inclusions on light scattering by large ice particles. *J Geophys Res* 1996;101(D18):23311–23316.
- [25] Hong G, Minnis P. Effects of spherical inclusions on scattering properties of small ice cloud particles. *J Geophys Res* 2015;120(7):2951–2969.
- [26] Xie Y, Yang P, Kattawar GW, Minnis P, Hu YX. Effect of the inhomogeneity of ice crystals on retrieving ice cloud optical thickness and effective particle size. *J Geophys Res -Atmos* 2009;114(D11).
- [27] Liu C, Panetta RL, Yang P. Inhomogeneity structure and the applicability of effective medium approximations in calculating light scattering by inhomogeneous particles. *J Quant Spectrosc Radiat Transf* 2014;146:331–348.
- [28] Jensen EJ, Toon O. The potential impact of soot particles from aircraft exhaust on cirrus clouds. *Geophys Res Lett* 1997;24(3):249–252.
- [29] Meano N. Air bubble formation in ice crystals. *Phys snow ice: Proc* 1967;1(1):207–218.
- [30] Mishchenko MI, Macke A. Asymmetry parameters of the phase function for isolated and densely packed spherical particles with multiple internal inclusions in the geometric optics limit. *J Quant Spectrosc Radiat Transf* 1997;57(6):767–794.
- [31] Cai Q, Liou KN. Polarized light scattering by hexagonal ice crystals: theory. *Appl Opt* 1982;21(19):3569–3580.
- [32] Takano Y, Jayaweera K. Scattering phase matrix for hexagonal ice crystals computed from ray optics. *Appl Opt* 1985;24(19):3254–3263.
- [33] Takano Y, Liou KN. Solar radiative transfer in cirrus clouds. Part I: single-scattering and optical properties of hexagonal ice crystals. *J Atmos Sci* 1989;46(1):3–19.
- [34] Takano Y, Liou KN. Radiative transfer in cirrus clouds. Part III: light scattering by irregular ice crystals. *J Atmos Sci* 1995;52(7):818–837.
- [35] Muinonen K. Scattering of light by crystals: a modified Kirchhoff approximation. *Appl Opt* 1989;28(15):3044–3050.
- [36] Macke A. Scattering of light by polyhedral ice crystals. *Appl Opt* 1993;32(15):2780–2788.
- [37] Plass GN, Kattawar GW. Monte Carlo calculations of light scattering from clouds. *Appl Opt* 1968;7(3):415–419.
- [38] Kattawar GW, Plass GN, Guinn Jr JA. Monte Carlo calculations of the polarization of radiation in the earth's atmosphere-ocean system. *J Phys Oceanogr* 1973;3(4):353–372.
- [39] Zhou C, Yang P, Dessler AE, Hu Y, Baum BA. Study of horizontally oriented ice crystals with CALIPSO observations and comparison with Monte Carlo radiative transfer simulations. *J Appl Meteorol* 2012;51(7):1426–1439.
- [40] Hu YX, Winker D, Yang P, Baum B, Poole L, Vann L. Identification of cloud phase from PICASSO-CENA lidar depolarization: a multiple scattering sensitivity study. *J Quant Spectrosc Radiat Transf* 2001;70(4):569–579.
- [41] Yang P, Liou KN. Geometric-optics-integral-equation method for light scattering by nonspherical ice crystals. *Appl Opt* 1996;35(33):6568–6584.
- [42] Yang P, Liou KN. Single-scattering properties of complex ice crystals in terrestrial atmosphere. *Contrib Atmos Phys* 1998;71(2):223–248.
- [43] Cox C, Munk W. Statistics of the sea surface derived from sun glitter. *J Mar Res* 1954;13(2):198–227.
- [44] Macke A, Mueller J, Raschke E. Single scattering properties of atmospheric ice crystals. *J Atmos Sci* 1996;53(19):2813–2825.
- [45] Liu C, Panetta RL, Yang P. The effective equivalence of geometric irregularity and surface roughness in determining particle single-scattering properties. *Opt Express* 2014;22(19):23620–23627.
- [46] Ulanowski Z, Kaye PH, Hirst E, Greenaway RS, Cotton RJ, Hesse E, Collier CT. Incidence of rough and irregular atmospheric ice particles from Small Ice Detector 3 measurements. *Atmos Chem Phys* 2014;14(3):1649–1662.

- [47] Czekala H. Effects of ice particle shape and orientation on polarized microwave radiation for off-nadir problems. *Geophys Res Lett* 1998;25(10):1669–1672.
- [48] Miao J, Buehler S, Kunzi K. The polarization characteristics of randomly oriented nonspherical ice particles in mm and sub-mm frequency range: Implications to the remote sensing of cirrus clouds using satellite microwave radiometry. In: *Proceedings of the IEEE 2001 International Geoscience And Remote Sensing Symposium*; 5: pp. 2442–2444; 2001.
- [49] Matrosov SY, Reinking RF, Kropfli RA, Bartram BW. Estimation of ice hydrometeor types and shapes from radar polarization measurements. *J Atmos Ocean Technol* 1996;13(1):85–96.
- [50] Cole BH, Yang P, Baum BA, Riedi J, C-Labonnote L, Thieuleux F, Platnick S. Comparison of PARASOL observations with polarized reflectances simulated using different ice habit mixtures. *J Appl Meteorol* 2013;52(1):186–196.
- [51] Riedi J, Goloub P. Comparison of POLDER cloud phase retrievals. *Geophys Res Lett* 2001;28(11):2185–2188.
- [52] Goloub P, Herman M, Chepfer H, Riédi J, Brogniez G, Couvert P, Seze G. Cloud thermodynamical phase classification from the POLDER spaceborne instrument. *Geophys Res Lett* 2000;105(D11):14747–14759.
- [53] Cole BH, Yang P, Baum BA, Riedi J, C-Labonnote L. Ice particle habit and surface roughness derived from PARASOL polarization measurements. *Atmos Chem Phys* 2014;14(7):3739–3750.
- [54] Hioki S, Yang P, Baum BA, Platnick S, Meyer KG, King MD, Riedi J. Degree of ice particle surface roughness inferred from polarimetric observations. *Atmos Chem Phys* 2016;16(12):7545–7558.
- [55] Baran AJ, Labonnote LC. On the reflection and polarisation properties of ice cloud. *J Quant Spectrosc Radiat Transf* 2006;100(1):41–54.
- [56] van de Hulst HC. Polarized light and asymmetry relations. In: van de Hulst HC, editor. *Light scattering by small particles*. New York: John Wiley & Sons; 1981. p. 41–57.
- [57] Jackson JD. Plane electromagnetic waves and wave propagation. In: Jackson JD, editor. *Classical Electrodynamics*. New York: John Wiley & Sons; 1975. p. 269–327.
- [58] Hansen JE, Travis LD. Light scattering in planetary atmospheres. *Space Sci Rev* 1974;16(4):527–610.
- [59] Bohren CF, Huffman DR. Absorption and scattering by a sphere. In: Bohren CF, Huffman DR, editors. *Absorption and Scattering of Light by Small Particles*. Wiley-VCH Verlag GmbH; 1983. p. 82–129.
- [60] Fu Q, Sun W. Mie theory for light scattering by a spherical particle in an absorbing medium. *Appl Opt* 2001;40(9):1354–1361.
- [61] Quinten M, Rostalski J. Lorenz-Mie Theory for Spheres Immersed in an absorbing host medium. Part I. *Syst Charact* 1996;13(2):89–96.
- [62] Yang P, Gao BC, Wiscombe WJ, Mishchenko MI, Platnick SE, Huang HL, Baum BA, Hu YX, Winker DM, Tsay SC, et al. Inherent and apparent scattering properties of coated or uncoated spheres embedded in an absorbing host medium. *Appl Opt* 2002;41(15):2740–2759.
- [63] Kattawar GW, Plass GN. Radiance and polarization of multiple scattered light from haze and clouds. *Appl Opt* 1968;7(8):1519–1527.
- [64] Ramella-Roman J, Prah S, Jacques S. Three Monte Carlo programs of polarized light transport into scattering media: part I. *Opt Express* 2005;13(12):4420–4438.
- [65] Stephens GL, Tsay SC, Stackhouse WP, Jr, Flatau PJ. The relevance of the microphysical and radiative properties of cirrus clouds to climate and climatic feedback. *J Atmos Sci* 1990;47(14):1742–1754.
- [66] Gerber H, Takano Y, Garrett TJ, Hobbs PV. Nephelometer measurements of the asymmetry parameter, volume extinction coefficient, and backscatter ratio in Arctic clouds. *J Atmos Sci* 2000;57(18):3021–3034.
- [67] Garrett TJ, Navarro BC, Twohy CH, Jensen EJ, Baumgardner DG, Bui PT, Gerber H, Herman RL, Heymsfield AJ, Lawson P, et al. Evolution of a Florida cirrus anvil. *J Atmos Sci* 2005;62(7):2352–2372.
- [68] Garrett TJ, Gerber H, Baumgardner DG, Twohy CH, Weinstock EM. Small, highly reflective ice crystals in low-latitude cirrus. *Geophys Res Lett* 2003;30:21.
- [69] Baran AJ. The dependence of cirrus infrared radiative properties on ice crystal geometry and shape of the size-distribution function. *Q J R Meteorol Soc* 2005;131(607):1129–1142.
- [70] Field PR, Baran AJ, Kaye PH, Hirst E, Greenaway R. A test of cirrus ice crystal scattering phase functions. *Geophys Res Lett* 2003;30:14.
- [71] Baran AJ. On the remote sensing and radiative properties of cirrus. In: *Light Scattering Reviews 2*. Berlin: Springer; 2007. p. 59–95.
- [72] Stegmann PG, Tropea C, Järvinen E, Schnaiter M. Comparison of measured and computed phase functions of individual tropospheric ice crystals. *J Quant Spectrosc Radiat Transf* 2016;178:379–389.
- [73] Iwabuchi H, Yamada S, Katagiri S, Yang P, Okamoto H. Radiative and microphysical properties of cirrus cloud inferred from infrared measurements made by the Moderate Resolution Imaging Spectroradiometer (MODIS). Part I: retrieval method. *J Appl Meteorol* 2014;53(5):1297–1316.
- [74] Cooper SJ, L'Ecuyer TS, Stephens GL. The impact of explicit cloud boundary information on ice cloud microphysical property retrievals from infrared radiances. *J Geophys Res Atmos* 2003;108(D3).
- [75] Nakajima T, King MD. Determination of the optical thickness and effective particle radius of clouds from reflected solar radiation measurements. Part I: theory. *J Atmos Sci* 1990;47(15):1878–1893.
- [76] Inoue T. On the temperature and effective emissivity determination of semi-transparent cirrus clouds by bi-spectral measurements in the 10  $\mu\text{m}$  window region. *J Meteor Soc Jpn* 1985;63(1):88–99.
- [77] Ryan BF. A bulk parameterization of the ice particle size distribution and the optical properties in ice clouds. *J Atmos Sci* 2000;57(9):1436–1451.
- [78] Riedi J, Marchant B, Platnick S, Baum BA, Thieuleux F, Oudard C, Parol F, Nicolas JM, Dubuisson P. Cloud thermodynamic phase inferred from merged POLDER and MODIS data. *Atmos Chem Phys* 2010;10(23):11851–11865.
- [79] Liu C, Panetta RL, Yang P. The effects of surface roughness on the scattering properties of hexagonal columns with sizes from the Rayleigh to the geometric optics regimes. *J Quant Spectrosc Radiat Transf* 2013;129:169–185.